

Dalton Transactions

Accepted Manuscript



This is an *Accepted Manuscript*, which has been through the Royal Society of Chemistry peer review process and has been accepted for publication.

Accepted Manuscripts are published online shortly after acceptance, before technical editing, formatting and proof reading. Using this free service, authors can make their results available to the community, in citable form, before we publish the edited article. We will replace this *Accepted Manuscript* with the edited and formatted *Advance Article* as soon as it is available.

You can find more information about *Accepted Manuscripts* in the [Information for Authors](#).

Please note that technical editing may introduce minor changes to the text and/or graphics, which may alter content. The journal's standard [Terms & Conditions](#) and the [Ethical guidelines](#) still apply. In no event shall the Royal Society of Chemistry be held responsible for any errors or omissions in this *Accepted Manuscript* or any consequences arising from the use of any information it contains.

ARTICLE

Cite this: DOI: 10.1039/x0xx00000x

Received 00th January 2012,
Accepted 00th January 2012

DOI: 10.1039/x0xx00000x

www.rsc.org/

A relationship among structural, electronic order-disorder effects and optical properties in crystalline TiO₂ nanomaterials

E. Silva Junior^{*a}, F. A. La Porta^a, M. S. Liu^b, J. Andrés^c, J. A. Varela^a and E. Longo^a^aLIEC, Instituto de Química, Universidade Estadual Paulista, P.O. Box 355, CEP. 14801-907 Araraquara, SP, Brazil.^bInstituto de Física de São Carlos, Universidade de São Paulo, P.O. Box 369, 13560-970 São Carlos, SP, Brazil.^cDepartment of Physical and Analytical Chemistry, Universitat Jaume I, Castelló de la Plana, 12071, Spain.

E-mail: euripedesj@gmail.com; Fax: +55 16 3301-9691; Tel: +55 16 3301-9892

The focus of this paper is on the analysis of the structural and electronic order-disorder effects at long, medium and short-range of titanium dioxide (TiO₂) nanoparticles synthesized by the sol-gel process which is followed by the microwave-assisted solvothermal (MAS) method at low temperatures and short reaction times. X-ray diffraction (XRD), Rietveld refinement, micro-Raman (MR) spectroscopy, transmission electron microscopy (TEM) and X-ray spectroscopy (EDX) were used to characterize the TiO₂ nanoparticles. Optical properties were investigated by ultraviolet-visible (UV-vis) and photoluminescent (PL) measurements performed at room temperature. XRD and Rietveld refinement confirmed the presence of the anatase and brookite phases, nonetheless anatase is the majority phase. X-ray photoelectron spectroscopy (XPS) analysis revealed the presence of only Ti⁴⁺ but the nonstoichiometry revealed that TiO₂ NPs contains defects assigned to oxygen vacancies that leads to structural and electronic order-disorder effects observed by band gap narrowing and PL wide band emission. These intermediary energy levels (shallow and deep levels) created within the band gap act as acceptors/donors of electrons and recombination centers. The oxygen vacancies (V_O^x, V_O[•] and V_O^{••}) responsible by degree of structural order-disorder are related to distortions (*tilts*) on the [TiO₆] octahedral and changes on the bond lengths and bond angles between oxygen and titanium atoms that gave to new species of clusters makers such as [TiO₆][•], [TiO₅.V_O^x], [TiO₅.V_O[•]] and [TiO₅.V_O^{••}]. This structural transformation is consistent with a redistribution of electron density from highly ordered [TiO₆]^x clusters which form distorted [TiO₆][•] as well as complex [TiO₅.V_O^x], [TiO₅.V_O[•]] and [TiO₅.V_O^{••}] clusters assigned to oxygen vacancies which were understood as displacements in the oxygen atoms position on the bond lengths (Ti-O).

Introduction

Titanium dioxide (TiO₂) is a versatile material which is utilized in a range of technological applications which embrace areas ranging from photovoltaics cells and photocatalysis to gas sensors.¹⁻⁴ TiO₂ properties depend strongly on particle size, crystal structure, morphology and crystallinity.⁵⁻⁷ Natural polymorphs of titania (TiO₂) include rutile (*P42/mnm*), anatase (*I42/amd*) and brookite (*Pcab*) with wide band gaps of 3.02, 3.20 eV and 2.96 eV, respectively. Each phase has unique physical properties, and phase transitions are dependent upon many factors such as particle size, morphology, pH, etc.⁸ Phase stability and phase transformation kinetics are substantially different in nanosized solids as compared to their bulk counterparts. A typical example of this phenomenon is that TiO₂ nanoparticles (NPs) have a stable rutile phase in bulk materials; however, the anatase phase becomes stable in TiO₂ NPs at a size

smaller than 14 nm⁹. The theoretical background to this phenomenon has been provided based on *ab initio* density functional theory (DFT) calculations.¹⁰

From a structural point of view, all three crystal structures consist of six-fold coordinated Ti atoms made up of [TiO₆] clusters and three-fold coordinated O atoms which share either edges or corners. The [TiO₆] octahedra can be considered as constituent clusters of TiO₂ but with different arrangements of neighboring and distorted [TiO₆] cluster-sharing oxygen atoms where they form three different crystallographic structures.¹¹⁻¹⁶ In this family, [TiO₆] octahedral clusters, in particular, exhibit marked structural flexibility and the structural distortion from rotation/tilting does not disrupt the corner-sharing connectivity in these frameworks. Galynska and Persson¹⁷ carried out quantum chemical calculations to show that the different TiO₂ forms of the three polymorphs can be clearly

distinguished based on structural characteristics associated with the local bonding environment of the constituent atoms.

As basic units, electronic structures of these clusters are drastically affected by structural order-disorder effects, and control of these lattice disorders in NPs is essential for developing nanomaterials tailored for specific optical properties and further applications. Only by probing these phenomena locally can we hope to link the structure and functionality of materials and thus open pathways for predictive modelling and synthesis. Very recently, Landmann and co-workers¹⁸ used the distorted [TiO₆] cluster and partial loss of this octahedral coordination as fingerprints of order and disorder in the electronic and optical properties of crystalline and amorphous TiO₂.

Properties, size and morphology of the as-synthesized nanomaterials are highly dependent on reaction conditions. TiO₂ nanostructures with various morphologies and sizes have been successfully synthesized using a variety of methods.^{12,19} In comparison with other methods, the sol-gel technique has advantages such as controllability, reliability and reproducibility which results in high quality and high purity materials.^{20,21} However, the polycondensation reaction of the sol-gel method, materials results in an amorphous phase or low degree crystallinity.²¹ Thus, it is necessary to perform a crystallization procedure; e.g. heat treatment by calcining, hydrothermal or solvothermal processes.

Among the modern techniques of synthetic chemistry, the microwave-assisted solvothermal (MAS) method is beneficial in all areas^{22a,b}. In particular, the use of microwave heating for the preparation of semiconductor nanomaterials has been employed due to its advantages over other synthetic methods. Primarily, the application of microwave irradiation on chemical transformations has been demonstrated to enhance reaction rates and cost effectiveness as well as to improve material quality and size distributions in nanomaterials and obtain cleaner reactions as compared to conventional routes.²³⁻²⁸ Because the mechanism and the microwave effects with synthesis are not well understood, this area is an open research field.²⁹⁻³¹ However, the MAS process promotes a nucleation-dissolution-recrystallization mechanism that is an order-disorder process which facilitates a non-classical crystallization process.³²

Within this context, an understanding of the formation of energy gaps is directly related to the nature of electronic and optical properties. The novelty of this work lies in the possibility that TiO₂ might be used as sources of blue and red light in light emitting devices in the future. Therefore, it is challenging and of scientific interest to obtain deeper insights into how structural and electronic properties can be related to short- and/or long-range order-disorder effects to explain optical properties of TiO₂ NPs obtained by a sol-gel process which is followed by the MAS method. To accomplish this deeper insight, XRD, Rietveld refinement, MR spectroscopy, TEM) and EDX analysis have been employed while optical properties were investigated by UV-Vis absorption and PL measurements. In addition, effects as well as the influence of the microwave heating by using the synthetic process are reported.

Experimental

Materials and methods

All chemicals were used as obtained without further purification. Titanium (IV) isopropoxide (97 % purity, Aldrich), ethyl alcohol anhydrous (99% purity, Fluka), hydrochloric acid (36.5 - 38 wt%, Merck) and deionized water (Milli-Q ultra-pure; resistivity

of 18.2 M Ω cm⁻¹) were maintained in a molar ratio of 1:20 and 0.75:4, respectively.

TiO₂ NPs were obtained by a two-step synthetic route based the on sol-gel process which was followed the by MAS treatment as follows: First, hydrochloric acid (3.11 mL) was added to ethyl alcohol (75 mL) with stirring for 15 min. Then titanium (IV) isopropoxide (14.8 mL) was added using an ultrasonic cleaner for agitation for 3 min.; a slightly yellowish transparent solution was produced which was stirred for 1 h. To promote the hydrolysis of metal alkoxide, deionized water (3.6 mL) was added to this solution while using an ultrasonic cleaner for 3 min. which resulted in a clear solution. The clear solution (linear polymer chains dispersed in the solvent) was placed into a sealed 100 mL Teflon[®] autoclave and loaded inside a non-commercial microwave oven which was operated at 2.45 GHz and 850 W of power. This system was processed at 120 °C under constant pressure (approximately 3.0 bar) for 2, 8 and 32 min with a heating rate of 10 °C min⁻¹. After heat treatment, a milky solution of TiO₂ NPs, was formed which was characterized by the formation of particulate gels. The nanoparticulate gels were dried at 50 °C to obtain xerogels which subsequently were crushed in a mortar to obtain a fine powder; the powder was calcined in a muffle furnace at 380°C for 12 h to remove organic matter.

Characterization

The structural analysis of the synthesized TiO₂ was performed by XRD using a Rigaku-DMax 2500PC (Japan) diffractometer at 40 kV and 150 Ma with Cu-K α radiation ($\lambda = 1.5406 \text{ \AA}$). The Rietveld routine was performed in the 2θ range from 10° up to 110° in a step-scanning mode was employed with a step width of 0.02° s⁻¹ and a fixed time of 1 s. The divergence slit used was fixed at 1°, and the receiving slit was established at 0.3 mm. Rietveld refinement method³³ was conducted using the *General Structure Analysis System* (GSAS) software designed by Larson and Von Dreele³⁴. The peak profile function was modeled using a convolution of the pseudo-Voigt with the asymmetry function described by Finger and Cox³⁵. The ICSD CIFs numbers 24276³⁶ and 31122³⁷ (ICSD – Inorganic Crystal Structure Database) were employed to obtain the best fit between theoretical profile and the measured profiles.

MR spectroscopy data were recorded using a T-64000 Jobin-Yvon triple monochromator coupled to a CCD detector. MR spectra were obtained using a 632.81 nm wavelength of an argon ion laser with its maximum output power maintained at 8 mw. A 50 μ m lens was used to prevent powder overheating, and MR data were taken with 30 s of acquisition time.

Morphologies were investigated by using TEM and EDX, and selected area diffraction (SAED) patterns were recorded on a JEOL 2100 transmission electron microscope operated at 200 kV. In the sample preparation for the TEM technique, the obtained powders were first dispersed in ethanol using an ultrasonic bath for 20 min, and then the suspensions were deposited on copper grids via fast immersion. The compositional analysis as well as the mapping of elements in analyzed samples was performed by EDX.

UV-vis spectra were taken by employing a Cary 5G spectrophotometer (Varian, USA) in diffuse reflectance mode. E_{gap} values were calculated by a method proposed by Kubelka-Munk method³⁸ where this energy is associated with diffuse reflectance measurements to estimate E_{gap} values with good accuracy (see Supporting Information). XPS was employed to determine the surface chemical composition and the oxidation states of the TiO₂ NPs. XPS spectrum were taken employing a UNI-SPECS UHV System operated at pressure less than 5x10⁻⁷Pa with an Mg-K α line (h ν = 1253.6 eV) ionization source and the pass energy of the analyzer set

to 10 eV. The inelastic noise of the high resolution spectrum for O 1s, Ti 2p, C 1s was subtracted by Shirley method.³⁹ The compositional atomic percentages of the surface layer (<5 nm) was determined by relative proportions of the spectrum areas revised by means of atomic sensitivity factors using a hydrocarbonates component corresponding to C 1s peak position around to 284.95 eV as the reference point. XPS spectrum was deconvoluted using a Voigt function (Gauss 70% and Lorentz 30 %) and the peak positions were determined within ± 0.1 eV of accuracy. PL spectra were measured in pellets at room temperature under an air atmosphere using a Monospec 27 monochromator (Thermal Jarrel Ash, USA) coupled to a R446 photomultiplier (Hamamatsu Photonics, Japan). A krypton ion laser (Coherent Innova 90 K, USA) ($h\nu = 350$ nm) was employed as an excitation source; its maximum output power was maintained at 500 mW and a maximum power of 40 mW on the sample after passing through an optical chopper.

Results and discussion

X-ray and Rietveld refinement data analyses

Long-range structural order is determined by XRD patterns which elucidate that the lattice of the TiO₂ NPs are formed by anatase (space group *I41/amd* in a *D_{4h}* symmetry) and brookite (space group *Pcab* in a *D₂* symmetry) which were indexed and are in good agreement with the ICSD CIF n° 24276 and CIF n° 31122. Fig. 1 displays the XRD patterns performed with Rietveld routine. The weak peak at diffraction position at $2\theta = 30.65^\circ$ is assigned to brookite orthorhombic structure for plane (121) while a strong peak at $2\theta = 25.32^\circ$ relating to the plane (101) of the anatase tetragonal. The others peaks diffracted also were indexed, however the broadening in the peaks, phenomenon usually found in system composed of nanoparticles⁴⁰, and the proximity of the diffracted peak position of some planes both anatase (A) and brookite (B) phases, thereby certain peaks might being ascribe to more of one plane. So, the others planes indexed were (101) A, (004) A, (200) A, (105) A or (320) B, (211) A, (204) A, (116) A or (400) B, (215) A, (224) A or (312) A, (217) A, (109) A and (316) A or (125)/(372)/(254) B. All planes indexed as well as their d-spacing, diffraction peaks position (2θ) and intensity are displayed with details in the Table S1 (see Supporting information). Therefore, the TiO₂ NPs are formed by two crystallographic structures, anatase and brookite, once the anatase phase is the major structure constituent in the TiO₂ NPs lattice.

Figure 1

Structural parameters were obtained from Rietveld refinements of XRD data and are displayed in Table 1. The Rietveld refinement method was employed to understand whether there are differences in the structural arrangements of TiO₂ NPs processed by MAS. The fit was performed using the least-squares approach by minimizing the sum of squares of differences between the theoretical values and the observed data.^{41a} The fit is conducted assuming the hypothesis that the reflections that contribute to profile can be simulated with the selected profile function.^{41b} Thus, the intensity value calculated in this process does not include the calculation of structure factors but is achieved by refining the values related to parameters of the peak-shape function selected for each reflection *hkl*, where the theoretical peak profiles are adjusted up to converge with the measured profiles.^{41c} The uncertainty in the derived weight fractions ascribed to each crystalline or amorphous phases beyond to the effects of preferred orientation, primary extinction, and nonlinear

detection systems can be minimized using all reflections in a pattern, rather than just the strongest ones.^{41d} Some criteria to judge the quality adjustments are required and therefore it is necessary to use some indices well-known like *R*-factors or Disagreement Factors (*R_p* - Profile Factor; *R_{wp}* - Weighted Profile Factor; *R_{exp}* - Weighted Profile Factor; *s*) Goodness of Fit Indicator and χ^2 - Reduced Chi-Square) which informs the each cycle, if refinement progresses satisfactorily and when it can be finalized with certain accuracy.^{42a} According to the literature^{42b,c} the data arising from structural refinements are generally checked by the quality algorithms or *R*-factors. However, the difference between the measured and calculated patterns might be a good way to verify the convergence of the refinement.

In this work, the parameters and coefficients optimized were scale factor, background (with function type : Shifted Chebyshev using 8 terms), sample displacement, Lorentzian coefficient to correct the sample broadening, size-strain (anisotropic no rules), Peak cutoff fixed at 3×10^{-4} to adjust the width of the peak base, microstructure, crystal structure, size-strain (anisotropic no rules), profile half-width parameters (*u*, *v*, *w*), lattice parameters (*a*, *b*, *c*), factor occupancy, atomic site occupancies (Wyckoff).^{42c,d} The adjustable parameters related to *R*-factors show good correlation between the simulated theoretical model and experimental data while lattice parameters and unit cell volumes are very close to results published in the literature.^{42b,42e}

The rapid TiO₂ formation process that governs microwave heating produces significant variations in *a*, *b* and *c* lattice parameter values and unit cell volumes. For TiO₂ NPs synthesized for 32 min, these distortions, stresses and strains yield a larger mass percentage (wt %) of the brookite phase (5.93 %, 5.60 % and 8.13 %) with 94.07 %, 94.40 % and 91.87 % of wt % assigned to anatase phase, for TiO₂ for NPs processed at 2, 8, and 32 minutes, respectively.

Table 1

A number of variations in atomic positions related to O and Ti atoms were observed which were independent of the time process for both anatase and brookite phases. We believe that these variations in atomic positions of atoms can result in the formation of distortions on the [TiO₆] octahedral cluster networks. Rapid heating with the MAS method causes structural defects due to distortions of the coordination polyhedra which are nanomaterials building blocks. This structural transformation is consistent with order-disorder effects in the crystal lattice as well as with redistribution of electron density from ideal [TiO₆] clusters to form distorted [TiO₅] clusters in the lattice. Table 1 shows the atomic position of the oxygen atom in the *z* coordinate of the 8e site which is displaced compared to the bulk coordinates of the anatase phase. For the brookite phase, displacements were observed for Ti and O atoms in the *x*, *y* and *z* coordinates of the 8c sites. We believe that the distortions on the coordination polyhedron is due to these displacements of the Ti and O atoms, therefore the bond lengths and bond angles in O-Ti-O undergo changes that can generate redistribution of electron density in the crystal lattice.

Micro-Raman analyses

To compare results obtained by XRD, we used Raman spectroscopy to evaluate the phase composition as well as the degree of order-disorder at short range of TiO₂ NPs. The information obtained by Raman scattering has been an excellent tool in the study of the formation of TiO₂ and titanates.⁴³⁻⁴⁹ The information related to the degree of order-disorder in the Raman spectrum is relative to the intensity, width and displacements of vibrational mode peaks.^{44,45}

Fig.2 shows MR spectra in the range from 50 cm^{-1} to 1000 cm^{-1} for TiO_2 NPs. Raman bands located around 144, 197, 399, 513, 519 and 639 cm^{-1} correspond to anatase vibrational Raman modes.⁴⁴ According to the symmetry group analysis of TiO_2 vibrational spectra, the anatase crystal structure has six Raman active modes ($A_{1g} + 2B_{1g} + 3E_g$); another three modes ($A_{2u} + 2E_u$) are infrared active; and one mode (B_{2u}) is inactive in the Raman or infrared region. For the brookite phase, Raman-active modes are located around 150, 323, 416 and 636 cm^{-1} , respectively.^{46,47} In particular, the width of the most intensive Raman band of brookite located at 154 cm^{-1} which can influence the width of the Raman mode of anatase structure at 144 cm^{-1} . The brookite phase must have vibrational mode characteristics with strong Raman scattering close to 128 (A_{1g}), 153 (A_{1g}), 247 (A_{1g}), 322 (B_{1g}), 366 (B_{2g}) and 636 cm^{-1} (A_{1g}), while the anatase phase already shows characteristic scattering at 146 (E_g), 396 (B_{1g}), 515 (A_{1g}) and 641 cm^{-1} (E_g).^{46,47} The spectrum shown in Figure 2 reveals that Raman bands of TiO_2 NPs were located at 144.3, 195.2, 394.8, 513.1 and 637.4 cm^{-1} , respectively.

Figure 2

Raman band values for TiO_2 NPs synthesized at 2, 8 and 32 min belong to anatase vibrational modes (E_{g1} , E_{g2} , B_{1g} , A_{1g} , B_{1g} and E_{g3}).⁴⁸ However, the positions of two modes (A_{1g} and B_{1g}) are not well defined in these Raman bands because there is an overlap of two modes and then a wide peak appears. In Raman scattering, the behavior of the dispersion slope from the scattering vector (q) is close to the Brillouin zone center ($q \approx 0$) for a given phonon mode which describes the nature of the association for a modification in the Raman line shape as a function of the crystal size.⁴⁹ A decrease in the crystal size facilitates a modification in the Raman line shape (negative slope) as well as a down-shifted or red-shifted Raman peak accompanied by increased broadening while an increase in the crystal size yields an up-shifted or blue-shifted Raman peak accompanied by a decreased broadening.^{47,48}

An analysis of Fig. 2 reveals that MR spectra associated with TiO_2 nanoparticles processed in 2, 8 and 32 min are very similar regarding the occurrence of red-shifted and blue-shifted peaks while peak broadening was not noticeable. Therefore, TiO_2 NPs crystal sizes are similar or are not capable of facilitating a modification in the Raman line shape. Thus, the presence of only six well defined Raman active modes ($A_{1g} + 2B_{1g} + 3E_g$) suggests that TiO_2 NPs for all synthesis times (2, 8 and 32 min) are ordered at long- and short-range with the anatase structure and there are no vibrational modes relative to other TiO_2 polymorphs. This conclusion is consistent with XRD results shown in Fig. 1.

TEM analyses

Morphologies of the synthesized TiO_2 products were studied by TEM. Figs. 3 (a, b, c) display HR-TEM image taken at higher magnifications. The first objective is to obtain a closer look at how these NPs are positioned on the carbon grid. Under higher magnification, nanocrystal agglomerates are observed and TiO_2 nanoparticles with an average size of approximately 10 nm. This result agrees with the fact that anatase is the most stable structure observed at the nanoscale, for particle sizes smaller than 14 nm.^{50,51}

Figure 3

SAED images (Figs. 3 (d, e, f)) reveals a polycrystal-type electron diffraction pattern with an interplanar distance of 0.35

nm which corresponds to the (101) plane of the anatase phase.^{52,53} The TiO_2 NPs morphology suggests that as-formed TiO_2 clusters are constructed of primary building particles with different orientations. The SAED from one of these zones confirms the presence of high crystallinity in both anatase and brookite phases which is in good agreement with XRD results.

The EDX is considered a qualitative or semi-quantitative technique able of the provide information about elemental composition and thus obtain the stoichiometry of the material, with detection limits of 0.1 wt%, depending of the atomic number of the atoms constituents.⁵⁴

Usually TiO_2 is a compound that presents an oxygen deficient on the lattice and commonly is represented as nonstoichiometric compound through of the formula TiO_{2-x} , where x is the effective deviation from stoichiometry (TiO_2).^{56a} Point defects in the crystals lattice may be created in the reduced or oxidized TiO_2 forms within simple phase regime. Under to reduced form, donor-types defects such as oxygen vacancies and titanium interstitials, might be created giving features of n-type semiconductor. While is expected a behavior of a p-type semiconductor under prolonged oxidation of the TiO_2 , due to presence of point defects assigned to titanium vacancies.^{56a,b} Therefore, the way more appropriate of represent the chemical formula of titanium dioxide, admitting deficit in both oxygen and cations sublattices, is thought of the formula $\text{Ti}_{1-x}\text{O}_{2-y}$, where Ti_{1-x} represents the titanium interstitials or titanium vacancies, while O_{2-y} is ascribed to oxygen vacancies.^{56b} However, the formula TiO_{2-x} is well accepted to represent the nonstoichiometry, once titanium interstitials are minority defects present in the bulk, subsurface or surface and are generates rather at elevated temperatures, i.e., by increasing annealing temperature.^{56c,d}

The stoichiometric composition from O:Ti ratio of the TiO_2 NPs was further confirmed by EDX (see Figs. 3 (g, h, i)) analysis and the values obtained were 1.99, 1.80 and 2.01 for the TiO_2 NPs processed in 2, 8 and 32 minutes, respectively. As can be observed by oxygen and titanium wt% results from EDX spectra, the TiO_2 NPs are nonstoichiometric compounds for samples processed at 2 and 8 minutes, while the O:Ti ratio for TiO_2 NPS processed at 32 minutes it seems to be most close to TiO_2 stoichiometry. Therefore, the nonstoichiometry observed by EDX results do not actually show a systematic variation of elemental composition as a function of processing time

The crystal growth process includes the nucleation and growth of particles. The particle size depends of the nucleation rate where a higher nucleation rate results in a smaller particle size.⁵⁷ Crystal growth by aggregation can occur by many mechanisms, including interactions of randomly oriented particles (i.e., coalescence) or highly oriented particles (i.e., oriented attachment).^{58,59} Our results indicate that the formation of these aggregates does not proceed via the classical ion-attachment mechanism, but by oriented aggregation of small primary subunits. As a consequence, this mechanism involves the formation of a high concentration of aggregated nanoparticles with the predominant growth controlled by the coalescence process.⁶⁰

In concentrated hydrochloric acid solutions, chloride ions, Cl^- , can be coordinated to the Ti^{+4} , but the complexes are not very stable⁶¹, consequently, chloride does not seem to have a specific role in titania crystallization. The influence of the Cl^- ions was investigated by Jolivet and co-workers.⁶⁰ They reported that Cl^- ions seem to be essential for brookite phase formation. Our results are in very good agreement with results obtained in other experimental studies.^{62,63}

Another important factor associated with acidic media is related to the mechanism of acidic catalysis in the condensation reaction for TiO₂ network formation in the sol-gel process. In this mechanism, titanium alkoxide is quickly protonated and decreasing the electron density of the metal atom (Ti⁴⁺) which becomes more electrophilic and more susceptible towards water attack and results in the formation of a penta-coordinated [TiO₅] transition state through a S_N² mechanism.^{20,21} Thus, in the MAS method, the crystal structure as well as the formation of anatase and brookite phases of the TiO₂ NPs in very acidic media seems to be controlled by the nature of the anions in the medium during processing. A similar argument was employed by Lee and co-workers⁶² to justify that the formation of anatase and brookite TiO₂ with various morphologies can be tailored by using various acid concentration. More recently, Moura and co-workers⁶⁴ obtained TiO₂ with the presence of the anatase and brookite phases by a similar solvothermal route, however the microwave time processing employed (1 to 60 minutes) promoted changes in the morphology (spheres and sticks) with micrometer size.

Optical properties and XPS analysis

The Kubelka-Munk method³⁸ was employed to calculate the optical band gap energy and is described in details in the Supporting information. The UV-vis spectra in Figure 4 shows a variation in the E_{gap} values from 2.71 to 2.98 eV (2, 8 and 32 min of heat treatment process times) which are lower than for anatase (3.20 eV).^{65a,b} These values depend mainly on preparation methods and experimental conditions such as precursor purity, processing time, etc. These key factors can advance or inhibit the formation of structural defects which are able to control the degree of structural order and disorder of the material and, consequently, the number of intermediary energy levels within the band gap⁶⁶ or due to a quantum effect.⁶⁷

Figure 4

We believe the decrease in the band gap value can be attributed to structural defects and local bond distortions according to results shown in the Tab. 1 (variation in the atomic coordinates of the Ti and O atom) and also due to the occurrence of a second phase assigned to brookite, as well as surface defects which are able to generate states with localized electronic levels within the forbidden band gap. Due to microwave effects in solvothermal conditions, parts of the material can crystallize, dissolve and recrystallize several times.^{22,68} This recrystallization process might lead to both surface and bulk modifications that change the structural order which is directly linked to rise of new energy levels in the band gap.

XPS is a powerful technique used to explore and characterize the presence of defects in bulk (<0.5 nm), thin films, surfaces and interfaces in the electronic structure studies. Besides studying the surface chemical composition and the oxidation states of the TiO₂ NPs, XPS was employed to investigate the presence of possible defects and the electronic structure by evaluation of the valence band (VB) in the low energy of the survey XPS spectrum (see Figure 5).

Figure 5

The XPS survey spectra of the TiO₂ nanoparticles processed for 2, 8 and 32 minutes by MAS method are shown in the Fig. 5 (a). The peaks observed above 900 eV correspond to Auger lines from O₂ (O KLL), Ti (Ti LMM) and C (C KLL). Despite

the presence of carbon (assigned to Auger line (C KLL) and the C 1s orbital), employed for the sample charging, no impurity related peak could be observed. All the values related to XPS survey spectra are shown with more details in the Table S2 (see supporting information). Fig. 5 (b) shows the high resolution spectra of the O 1s core level spectra de-convoluted into three symmetric peaks using an asymmetric Gaussian-Lorentzian function fit. The profile of the O 1s XPS spectra, for all samples, consists of a main peak at 530.06 eV that corresponds to the crystal oxygen lattice in O²⁻ bound to Ti⁴⁺; minor peaks with at 531.42 and 532.34 eV are assigned to oxygen vacancies⁶⁹ and surface hydroxyl groups.^{70a,b} FWHM (full width at half maximum) and % area values of the de-convoluted peaks respect to Ti 2p and O 1s XPS signals are exhibited in the Table S3 (see Supporting information). Fig. 5 (c) shows the Ti 2p XPS spectra composed of two peaks assigned to signals Ti 2p_{3/2} and Ti 2p_{1/2} localized at 458.77 and 464.51 eV, respectively, with a peak separation average of 5.75 eV assignable to Ti⁴⁺ ions in TiO₂.^{71a-d} In the typical XPS spectra profile, the binding energy of Ti 2p XPS signals, for stoichiometric TiO₂, are not broad and there are no shoulder peaks.⁷² However, in sub-oxides (TiO₂, Ti₂O₃, Ti₅O₃, TiO Ti₂O, Ti₃O) may be present with different oxidation state (Ti²⁺, Ti³⁺ and Ti⁴⁺) depending of the stoichiometry.^{73a-c} The sub-oxide species are comparatively lower in concentration as opposed to the normal oxidation state Ti⁴⁺. Through appropriate Gauss-Lorentzian fitting, the Ti 2p XPS spectra can be used to obtain information about the oxidation states of the sub-oxides containing Ti³⁺, Ti²⁺, Ti⁺ and Ti⁰ ions on the surface of reduced TiO₂.⁷² Fig. 5 (c) illustrates the shape and position (values noted in Supporting information) of the Ti 2p_{3/2} XPS signals which, independent of the processing time, the absence of broad and shoulder peaks makes it reasonable to conclude that only Ti⁴⁺ species are bound to O²⁻ in the TiO₂ lattice^{73b} on the surface TiO₂ NPs, once Ti³⁺ surface defects and Ti²⁺ shown by Ti 2p_{3/2} peaks located at 457.7 and 454.4 eV, respectively, are absent.^{73b-d} The O 1s and Ti 2p area (Table S2 Supporting information) for these TiO₂ NPs can be used to determine the O:Ti ratio (as determined by XPS peak areas) and thus establish the stoichiometry. The results in Tab. S2 show that the O:Ti ratio for TiO₂ NPs processed in 2, 8 and 32 minutes were 2.48; 2.47 and 2.55 respectively, not as expected for TiO₂. However, considerations can be made regarding the O 1s XPS signals for a more realistic interpretation Regonini and co-workers⁷⁴ determined the value of approximately 3 for the oxygen to titanium ratio (O:Ti) of the oxide films, for which contributions of the O 1s XPS signals localized at 531.4 and 533.1 eV, were ascribed to hydroxyl groups (probably some organic contaminants) and oxygen from isopropanol bonding with the outer oxide layer, respectively. Therefore, neglecting the contribution due to oxygen from water/hydrated species and from organic origins the O:Ti ratio decreases to approximately 2.4 suggesting that the oxide films not purely TiO₂, but rather hydrated TiO₂. In our work, also neglecting the contribution of the components from O 1s XPS signals assigned to oxygen vacancies (531.42 eV) and hydroxyl groups (532.34 eV), the O:Ti ratio decreases to approximately 2.26, 2.21 and 2.21 for TiO₂ NPs processed in 2, 8 and 32 minutes, respectively, once only approximately ≈ 79% of the O 1s XPS signals is related to O²⁻ bound to Ti⁴⁺ in TiO₂ form (see Table S2 Supporting information).

The values obtained by EDX TEM for the stoichiometric composition (see Figs. 3 (b, d, f)) were 1.99, 1.80 and 2.01, for TiO₂ NPs processed in 2, 8 and 32 minutes, respectively,

whereas XPS analyses obtained 2.26, 2.21 and 2.21, for the same samples. Thus as the O:Ti ratio observed by EDX results, also from XPS results do not able of to show a systematic variation of elemental composition as a function of processing time. These deviations observed might be related to qualitative nature of the EDX technique and by the fact that EDX to be more representative of the bulk than surface⁵⁴ whereas XPS is a technique most sensitive to surface chemical analysis which can detect the compositional samples, in atomic content (at%), up to 10 nm of thickness.⁷⁵ Hence, the absorbed species such as hydroxyl groups and probably some organic contaminants might be strongly bound to TiO₂ NPs. Since the physically absorbed species on the TiO₂ surface can be easily eliminated by XPS conditions, under a ultrahigh vacuum system, a purely TiO₂ single crystal or TiO₂ with a fine surface structure will not show XPS signals.^{76,77} However, the complexity of bound hydroxyls no allows that XPS analysis is suitable of provide an analysis more detailed about to surface hydroxyl groups bound to TiO₂ surface

Therefore, as was not detected by XPS analysis of the Ti 2p peaks, the presence of Ti³⁺ which is assigned to surface defects in the TiO₂, we believe that TiO₂ NPs contains a disorder at interface such as surface and/or grain boundaries, by the fact that nanosized TiO₂ materials exhibit a large interface-to-volume.^{69,78} For anatase, generally the surface states are oxygen vacancies or Ti⁴⁺ ions adjacent to oxygen vacancies.^{79a,b} The rise of the oxygen vacancies will be discussed later in details.

A brief and qualitative evaluation of the VB spectra, shown in the Fig 4 (d), is a helpful tool to assist understanding of the rise of the defects state. This fact plays an important role to a better understand the optical behavior for these TiO₂ NPs. As is well-known, pure anatase TiO₂ has primarily a filled VB derived mainly from O 2p (2p_x, 2p_y and 2p_z) orbitals separated from an empty conduction band (CB) derived from Ti 3d orbitals (3d_{x²-y²}, 3d_{z²}, 3d_{yz}, 3d_{zx} and 3d_{xy}) by a bulk band gap of 3.2 eV.^{65a,b} Sm³⁺-doped TiO₂⁸⁰ with anatase and rutile crystal structures showed a different electronic structure, where impurity energy levels were created from Sm-4f states hybridized with the O 2p states above the VB and other Sm-related energy levels located in the energy range of -3–0 eV, for the anatase crystal structure. The Sm³⁺-doped TiO₂ for rutile, Sm-related impurity energy levels are localized at the CB in the energy range of 4–6 eV. Therefore, the structural order assigned to crystal structure (anatase and rutile) determined the behavior of the electronic structure associated with Sm³⁺-doping. The VB displays (Fig. 5(c)) show the same behavior of the electronic structure for the TiO₂ NPs processed for 2 and 8 minutes, in which the electronic structure is close to Fermi edge. However, the presence of the shoulder close to the Fermi edge is most evident for TiO₂ NPs processed for 32 minutes. The shift of the Fermi level arises from the defects state found at the top of the VB, as observed by a decrease in the optical band gap energy which is in good agreement with UV-vis results.

In terms of the optical properties, the E_g involves the surface and bulk contributions which are assignable to the arrangement of the energy levels within band gap.^{81a-c} Despite the properties that arise from of creating of intermediary energy levels within the band gap are commonly found in doped semiconductor materials, undoped materials processed by a specific synthetic method may present these properties due to a degree of structural disorder at short, medium or long-range.^{82a,d} We believe that TiO₂ NPs processed for 32 minutes undergo more recrystallization steps under hydrothermal conditions via

microwave heat than TiO₂ NPs processed in 2 and 8 minutes, leading to a larger structural disorder able of to create a slightly larger concentration defects that promotes the arrangement of the intermediary energy levels within the band gap. Since the factors such as preparation method, particle morphology, heat treatment temperature and processing time are factors that promote changes in the different structural defects such as formation of oxygen vacancies, modifications on the bond lengths, changes on the dihedral angles and distortions on the clusters which may give rise to intermediary energy levels within the band gap.^{82b}

Therefore, the Fermi level is shifted (Fig. 4(d)) by arrangement of the intermediary energy levels at top of the VB which the degree of structural order-disorder at leads to structural disorder at long-range due to symmetry breaking, by presence of the brookite phase (shown by XRD and Rietveld refinement), whereas at short-range by MR results it appears that TiO₂ NPs structure is more ordered.

UV-vis spectroscopy is a technique that can be combined with PL spectroscopy to understand the density of structural defects which are able to generate intermediary energy levels within the band gap and control the degree of structural order-disorder in the lattice.^{82a} PL spectroscopy is very useful to obtain information about electronic, optical and photoelectric properties of materials.^{83,84}

PL studies might provide information on the structure, defects and impurities in a material^{82a-d}. PL properties are a powerful probe for investigating changes around the site environment at short-range (2–5 Å) and medium-range order (5–20 Å) of clusters where the degree of local order is pronounced.^{66,82a,c} Structurally inequitable sites can be distinguished because of their different types of electronic transitions that are linked to a specific structural arrangement.^{65(a,d)82a-d} In this context, we can understand the nanostructural problem as pointed out by Billinge and Levin⁸⁵ about existing problems in determining the atomic structure of nanomaterials “we don't have robust broadly applicable quantitative methods for solving structures at the nanoscale, and this is precisely the domain where the crystallographic methods lose their power”.

PL measurements demonstrate energy transfer processes where specific structural rearrangements occur. PL emissions can be related to several factors that changes electrons transitions in the band gap; i.e. by defects related to stresses and strains on the lattice (*tilts*),^{86a} cation or anion vacancies,^{86b,c} surface states^{86d} and quantum confinement.⁶⁷ Defects that produce deep levels generate intermediary energy levels near the CB are represented by PL emission at low energy (yellow/red),^{86b,c} while shallow levels generate states next to the VB that exhibit PL emission in regions of high energy (violet/blue).^{86a}

Fig. 6 (a) illustrates PL spectra of TiO₂ NPs at room temperature and under an air atmosphere. The PL spectrum covers visible electromagnetic signals in the range from 400 to 800 nm; these spectra are broad and are typical of a multiphonon process; i.e., a system where relaxation occurs by several paths involving the participation of numerous states within the band gap of the material.^{82a,86d}

Figure 6

Therefore, the PL emissions cannot be ascribed to the direct recombination process between a conduction band electron in the Ti 3d orbital and a hole in the O 2p valence band. The wide band profile of the observed PL behavior is associates with several radiative and/or non-radiative luminescent centers

generated from defect density. The structural disorder in the crystal lattice promotes a polarization effect due to redistribution of electron density by changes in the bond lengths and bond angles between Ti and O atoms resulting in the non-uniform electronic structure.

An analysis of PL spectra (see Fig. 6 (a)) shows that TiO₂ NPs has a maximum emission associated with PL emissions at 539 nm, 534 nm and 528 nm, for 2, 8 and 32 minutes of time processing, respectively. Therefore, the PL emission bands are slightly displaced in function of processing time. The wide PL bands emissions show a blue shift between PL emission bands for 2 and 8 minutes and red shift between PL emission bands for 8 and 32 minutes. The PL shift seem to indicate that concentration and the nature of the defects created into TiO₂ NPs, depending to degree of structural order-disorder which is intimately related to processing time of heat treatment.

It appears reasonable to correlate the PL energies to intermediary energy levels within the band gap⁶⁹, once the PL emissions localized at approximately at 530 nm (≈ 2.34 eV) is lower than experimental band gap.

To gain a deeper insight regarding the emissions, the PL spectrum was deconvoluted with a Voigt function using the PeakFit program (4.05 version).⁸⁷ The PL spectra can be deconvoluted into three peaks (PL sub-bands), which are centered at 451, 523 and 605 nm, and are ascribed to components in the blue, green and orange regions, respectively. Each component contributes to the wide band profile and is linked to a specific structural defect. The analysis of the deconvoluted peaks (see Fig. 6 (b-d)) confirms that the variation in emission intensity (% area) of the components (blue, green and orange) can be explained by the variation in the defects density created during the processing time employed in the MAS method.

PL behavior for TiO₂ anatase is associated with three kinds of physical origins: self-trapped excitons (STEs),⁸⁸ oxygen vacancies⁸⁹ and surface states.⁹⁰ The PL band localized in the ultra-violet (violet/blue) are characteristic of an intrinsic luminescence, i.e. structural defects, that cause distortions on the coordination polyhedron hexa-coordinated [TiO₆] clusters of the anatase,^{86a,88} whereas extrinsic luminescent emissions are situated at low energy (green/yellow) and are associated with oxygen vacancies and surface states.^{86b-d}

According literature^{82b} the factors related to preparation method can promotes a degree of structural disorder able of give rise to different structural defects. The internal/external vibrational between clusters adjacent strongly bound provide information about the degree of structural order-disorder in the lattice.^{82c,90} Nonetheless, the symmetry breaking these clusters leads to distortions on the clusters, modifications on the O–Ti–O bond lengths, changes on the dihedral angles and formation of oxygen vacancies.^{90,91} Hence we believe that the degree of structural disorder related to symmetry breaking due to brookite phase as well as heat treatment from MAS method, might being responsible by distortions (*tilts*) on the [TiO₆], changes on the O–Ti–O bond lengths and formation of oxygen vacancies, which latter could act as donors for charge carriers, trap sites of electrons, and/or recombination centers.⁶⁹

It is well-established that the relationship between the degree of structural order-disorder in the bulk and surface^{81a-c} contributes to the wide band profile^{82a-c} observed which can be distinguished by degree of the perturbation contained on the TiO₂ NPs lattice at short, medium or long-range.

Bond lengths and bond angles between titanium and oxygen atoms from the atomic coordinates obtained by Rietveld refinements results are displayed in the Table S4 (see

Supporting Information). The bond lengths and bond angles values were calculated through Visualization for Electronic and Structural Analysis (version 3 for Windows),⁹² and the unit cell parameters of the ICDS CIF n° 24276 and CIF n° 31122 were used as reference.^{36,37} The results show that [TiO₆] clusters, both anatase and brookite, are slightly distorted on the cell unit, by variation in the bond lengths (Ti–O_n (n = 1,...,6)) and the bond angles, formed between two oxygen atoms and the titanium atom (ψ , ϕ , φ , ε , γ and δ), on the TiO₂ NPs lattice. As the crystallization process proceeds during the processing time, the several crystallization steps under hydrothermal conditions aided by the fast heat of the MAS method promote a structural arrangement for each crystallization step by shifting the atomic coordinates of the oxygen and titanium atoms, thus obtaining a network formed by distorted clusters that leads to a symmetry breaking, resulting in an asymmetric charge distribution^{82a-c} in the intermediate-range order which confirms additional electronic levels within the band gap. By comparing the results obtained by the Rietveld refinement (see Table 1), and the deviations in the bond lengths and bond angles compared to theoretical values and the deconvolution of the PL spectra (see Fig. 6 (b-d)), it reasonable conclude that there is a degree of structural disorder due to symmetry breaking^{82c,90} linked to oxygen vacancies, with different charged states (V_O[•] and V_O^{''}) or in a neutral state (V_O^x)⁹³, that acts on the arrangement of the energy levels within the band gap region leading to changes the electron density in TiO₂ NPs crystal lattice, where each PL sub-bands (blue, green and orange) is related to one kind of electronic transition between the several energy levels created within the band gap.

The ordered–disordered of the TiO₂ and titanate structures, can leads to an ordered structure with [TiO₆] clusters makers, and another disordered structure which is ascribed to [TiO₆] slightly distorted and another [TiO₅] complex clusters, which all are related to an specific type of oxygen vacancies.^{91,93} Hence, two effects which are attributable to TiO₂ NPs PL behavior can be identified from the degree of structural order-disorder due to defects ascribed to oxygen vacancies on the TiO₂ NPs network. The first effect emerges from the deformations (*tilts*) induced on the [TiO₆] octahedral clusters and deviations on the bond lengths that promotes a slight shift in the the oxygen atom position that give rise to intermediary energy levels within the band gap which are responsible for luminescent centers at high energy (blue component).^{86a,88} The second effect is derived from a displacement slightly larger in the oxygen atom position that might be understood as defect near at surface, not assigned to presence of Ti³⁺ sites but those, *i. e.* due to surface dangling bonds⁶⁹, resulting in another type of oxygen vacancy on the TiO₂ NPs lattice which are represented by [TiO₅] complex clusters. This second effect also promotes narrowing in the optical band gap energy by generating intermediary energy levels within the band gap, which are responsible for the low energy luminescent centers (green and orange components).^{86b,c} The mechanism shown in Fig. 7 explains the PL behavior at room temperature of TiO₂ NPs processed by the MAS method for different processing times.

Figure 7

Bulk, surface and interface defects may be possible trap sites for charge carriers^{81a-c,82a}. Temperature-variable PL of the TiO₂ nanotube highly crystalline, as a function of wall thicknesses ~ 20 nm, show that at low temperature (< 50 K)

electrons would occupy the trap sites without thermal excitation, hence STEs becomes predominant in the direct relaxation, while at high temperature (> 50 K) due to the thermal quenching by non-radiative recombination, STEs is suppressed by oxygen vacancy states.⁶⁹

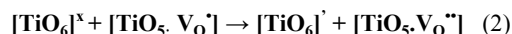
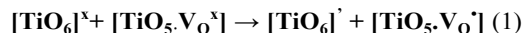
Therefore, disorder generates imbalanced charges on the structure and leads to formation of electrons and holes in the TiO_2 NPs lattice. During the excitation process in the crystals, the electronic transitions involve more than one kind of cluster on the lattice where the charge transfer takes place between clusters^{81(b,c)}, whereas in relaxation process the recombination of excitons might be trapped by energetic states within the band gap^{82a} or might be trapped/detrapped in sites into $[\text{TiO}_6]$ clusters generates from local distortions on the lattice assigned to a specific phonon mode^{69,94}. However, the increasing of temperature promotes the decreasing or extinction of the defects assigned to structural local disorder in the lattice.

The assumption is made that one oxygen vacancy is not necessarily linked to an insufficiency of oxygen atoms on the TiO_2 crystal lattice but rather, a displacement in the oxygen atomic position leading to a polarization effect. The bond lengths (Ti-O) increase, which is the charge transport in the crystal lattice. Fig. 7 shows a scheme of oxygen vacancy types that might be present in the TiO_2 NPs lattice.

Figure 8

The picture shows only two $[\text{TiO}_6]$ adjacent clusters, but the model extends to the surface and all bulk NPs. In (1), the $[\text{TiO}_6]$ clusters shows the oxygen atom position representing the most structurally ordered arrangement of the TiO_2 crystal lattice without oxygen vacancies. It is assumed that the no vacancy condition refers to the structural arrangement using the bond lengths (Ti-O) and bond angles (O-Ti-O) of the theoretical values of the anatase (ICDS n° 24276) and brookite (ICDS n° 31122) phases. In (2) the oxygen atom, between two adjacent clusters, refers to a structural arrangement which is assigned to neutral oxygen vacancy (V_O^\times) that despite representing the still ordered structure, the oxygen atom position is slightly displaced compared to the theoretical structural arrangement position 1. Therefore, a slight polarization⁹¹ begins to emerge. In (3), increases in the bond lengths (O-Ti) or distortions (*tilts*) on the $[\text{TiO}_6]$ octahedral cluster begin to redistribute the charges in the crystal resulting in two regions with slightly different electronic density. The electron will be closer to the $[\text{TiO}_6]$ cluster where the distortion is larger or in the cluster where the oxygen atom will be closest to forming the single ionized ($\text{V}_\text{O}^\bullet$) oxygen vacancy. When the distortions or bond lengths increase to a still larger displacement (4), of the oxygen atom, a polarization effect, due to the larger charge separation, might occur creating a high electronic density region (HED) and another with low electronic density region (LED). For this effective polarization effect the oxygen vacancy double ionized ($\text{V}_\text{O}^{\bullet\bullet}$) is associated. In positions 2, 3 and 4, the increase of the displacement of the bond length (Ti-O) followed by one sharp distortion on the $[\text{TiO}_6]$ octahedral gives rise to complex $[\text{TiO}_5]$ clusters, represented by $[\text{TiO}_5\text{V}_\text{O}^\times]$, $[\text{TiO}_5\text{V}_\text{O}^\bullet]$ and $[\text{TiO}_5\text{V}_\text{O}^{\bullet\bullet}]$ species respectively, unlike as in picture 1 in which the network is formed only by $[\text{TiO}_6]^\times$ clusters. Therefore, instead of the idea of insufficient oxygen atoms⁹⁵, the oxygen vacancies V_O^\times , $\text{V}_\text{O}^\bullet$ and $\text{V}_\text{O}^{\bullet\bullet}$ on the TiO_2 NPs can be understood by bond length displacement (Ti-O) able of promotes distortions on the TiO_6

octahedral clusters as well as modifications on the bond lengths bond angles or dihedral angles, and are associated with $[\text{TiO}_6]^\times$ clusters, that represents the most ordered TiO_2 structure, according to the following equations:



Equations (1) and (2) show the transformation of the TiO_2 highly ordered structural neutral network, formed by $[\text{TiO}_6]^\times$ - $[\text{TiO}_6]^\times$ clusters, to a slightly polarized network formed by $[\text{TiO}_6]^\bullet$ - $[\text{TiO}_5]$ due to structural disorder arising from oxygen vacancies V_O^\times , $\text{V}_\text{O}^\bullet$ and $\text{V}_\text{O}^{\bullet\bullet}$. The $[\text{TiO}_6]^\bullet$ clusters, unlike $[\text{TiO}_6]^\times$, are a distorted octahedral that give rise to a slight polarization effect in the TiO_2 NPs crystal lattice when the oxygen atom displacement becomes larger as compared to position 1, and/or as soon as the *tilts* increases. The relationship between defects and PL observations can be understood by noting the concentration of the markers species of the TiO_2 NPs network, i.e. $[\text{TiO}_6]^\times$, $[\text{TiO}_5\text{V}_\text{O}^\times]$, $[\text{TiO}_6]^\bullet$, $[\text{TiO}_5\text{V}_\text{O}^\bullet]$ and $[\text{TiO}_5\text{V}_\text{O}^{\bullet\bullet}]$. The concentration of these species is based in the dynamic of the transformation of the $[\text{TiO}_6]$ clusters, represented by $[\text{TiO}_6]^\times$ and $[\text{TiO}_6]^\bullet$ to complex $[\text{TiO}_5]$ clusters, represented by $[\text{TiO}_5\text{V}_\text{O}^\times]$, $[\text{TiO}_5\text{V}_\text{O}^\bullet]$ and $[\text{TiO}_5\text{V}_\text{O}^{\bullet\bullet}]$.

Therefore, the TiO_2 NPs network is formed by a relationship between structural order-disorder induced by oxygen vacancies that at long range, distorted $[\text{TiO}_6]^\bullet$ and complex $[\text{TiO}_5\text{V}_\text{O}^\times]$ clusters are assigned to interface anatase/brookite phases and *tilts* on the $[\text{TiO}_6]$ octahedral and slight changes on the bond lengths and bond angles between oxygen and titanium atoms, that give rise to shallow levels within the band gap close to CB responsible for luminescent centers at high energy, and by complexes $[\text{TiO}_5\text{V}_\text{O}^\bullet]$ and $[\text{TiO}_5\text{V}_\text{O}^{\bullet\bullet}]$ clusters which might be understood as dangling bonds defect near at surface, giving rise to deep levels within the band gap close to VB responsible by PL emissions at low energy. Both shallow and deep levels might acts to as acceptors/donors for charge carriers, trap sites of electrons, and/or recombination centers. While at short-range the TiO_2 NPs structure is more ordered, once the increasing of processing time no promotes local distortions able of changes the periodic spacing in the $[\text{TiO}_6]$ octahedra, due to the presence of only phonon active-modes Raman assigned to vibrational intrinsic of the anatase lattice for all TiO_2 NPs. Other hand, the TiO_2 NPs lattice is formed by a network from interactions between different clusters makers (as shown in Fig. 8), so it seems reasonably conclude that at medium-range there is a slight degree of structural disorder caused by distortions in the dihedral angles^{82c,90} between clusters adjacent, once for an ordered structure the dihedral angles is related to equilibrium position between ordered clusters $[\text{TiO}_6]^\times$ - $[\text{TiO}_6]^\times$, however the clusters makers of the disordered structure of the TiO_2 NPs are $[\text{TiO}_6]^\times$ - $[\text{TiO}_5\text{V}_\text{O}^\times]$, $[\text{TiO}_6]^\bullet$ - $[\text{TiO}_5\text{V}_\text{O}^\bullet]$ and $[\text{TiO}_6]^\bullet$ - $[\text{TiO}_5\text{V}_\text{O}^{\bullet\bullet}]$ which the bond lengths (Ti-O) and bond angles (O-Ti-O) are

slightly distorted, hence exhibit distortions in the dihedral angles.

Oxygen vacancies on the disordered structure^{82c,91,93} work like electron trapping or hole trapping centers which generate intermediary levels within the band gap according to the equations (2) and (3), where $[\text{TiO}_6]^\cdot$ is the donor, $[\text{TiO}_5, \text{V}_\text{O}^\cdot]$ is the donor or acceptor, and $[\text{TiO}_5, \text{V}_\text{O}^{\cdot\cdot}]$ is the acceptor; $[\text{TiO}_5, \text{V}_\text{O}^{\cdot\cdot}]$ is a neutral complex with two unpaired electrons; $[\text{TiO}_5, \text{V}_\text{O}^\cdot]$ has one unpaired electron; and $[\text{TiO}_5, \text{V}_\text{O}^{\cdot\cdot}]$ has no unpaired electrons. These equations suggest that electrons trapped (+) in an oxygen vacancy complex are a necessary requirement for the formation of polarons during the excitation process that changes the electronic density of the crystal causing a polarization effect.^{91,93,96} Similar arguments have been used very recently to represent oxygen vacancies in the case of SnO_2 quantum dots.⁹⁷

It was proposed a wide band model (Fig. 8) based on the electronic transitions that might occur between the intermediary energy levels in order to explain the origin of the PL emissions for TiO_2 NPs. In the PL model proposed, an important step occurs before the excitation process that strengthens the argument about to intermediary energy levels created within the band gap. Before the excitation process (Fig. 8a), deep levels are created close to the VB and thus the electron might occupy these levels (an excited state (S^*)), changing the electronic arrangement. Therefore, when the electrons occupy these energy levels close to the VB, this electronic arrangement is defined as the ground state since no energy source (electromagnetic) acts under TiO_2 NPs, only thermal energy at room temperature. Hence, the excitation of the crystal lattice might occur via phonons. After being excited (Fig. 8b) by an energy source ($h\nu$), positive holes (h^\cdot) in the S^* and negative electrons (e^\cdot) are created in the CB or in some intermediary energy levels (shallow levels) close to CB. Thus, charge carriers and trap sites are presents in the hole-electron (e^\cdot - h^\cdot) recombination pairs to explain the PL behavior of TiO_2 NPs that occur from mechanism where:

- (1) the positive holes created in the S^* , after the electron to be excited, can be electrostatically attracted by electron trapped by shallow levels close to the CB generating an exciton pair which due to their instability suffers annihilation via radiative decay ($h\nu_1$);
- (2) once light source excitation energy (laser $\lambda=354$ nm) is greater than optical band gap energy (see UV vis results) there is possibility that the electron localized at S^* is not be trapped by deep levels close to VB, but rather to be excited toward the CB by band-band transition which fall back again to deep levels via radiative decay ($h\nu_2$);
- (3) once at CB the electron might undergo recombination toward shallow levels closest to the CB via radiative decay $h\nu_3$ and keep successive relaxation processes falling back again to adjacent deep levels via radiative decays $h\nu_3, h\nu_4, \dots, h\nu_n$.

Therefore, the energies arising from all these electronic transitions are converted in photons ($h\nu$), which the several photons ($h\nu_1, h\nu_2, h\nu_3, h\nu_4, \dots, h\nu_n$) originated during the multiple radiative electronic transitions are responsible by the PL wide band emissions^{82a-c,90,91,93,96}

The concentration of intermediary energy levels (shallow and deep levels) within the band gap is related to concentration of

defects generated by degree of structural order-disorder from oxygen vacancies ($\text{V}_\text{O}^{\cdot\cdot}, \text{V}_\text{O}^\cdot$ and $\text{V}_\text{O}^{\cdot}$). According the deconvolution of the PL spectra, the contribution of each PL sub-bands (blue, green and orange) occurs in a random way, i.e., is not related to the processing time of the TiO_2 NPs. However, the contribution (% area) of the PL sub-bands (green and orange) is larger than blue component. Therefore, it seems reasonable conclude that the PL behavior is dominated by luminescent centers responsible by PL emission at low energy. Hence, the concentration of deep levels within the band gap is larger than shallow levels, once defects arisen from structural disorder assigned to $[\text{TiO}_5, \text{V}_\text{O}^\cdot]$ and $[\text{TiO}_5, \text{V}_\text{O}^{\cdot\cdot}]$ complex clusters are responsible by PL sub-bands at green and orange. So, the concentration of these species on the TiO_2 NPs lattice is larger.

4. Conclusions

From a quantitative analysis of the results, we have confirmed in this study a correlation among structural, electronic order-disorder effects at long, medium and short-range and their optical properties for TiO_2 nanoparticles synthesized by the sol-gel process which is followed by the MAS method. During the sol-gel conventional process, without any heat treatment, the formation of connections along the network of $[\text{TiO}_6]$ clusters, via Ti-O-Ti, is very slow. However, when the MAS method is employed, the Ti-O-Ti bond formation is promoted by a cooperative effect related to hydrolysis and condensation reactions resulting in TiO_2 NPs with a particular structure composed by distorted lattices. The microwave assisted solvothermal process showed that only in 2 minutes it was possible obtain TiO_2 NPs with highly oriented particles (oriented attachment).

The fast microwave heat process under hydrothermal conditions was able to promote rearrangement of the atomic coordinates of the oxygen and titanium atoms leading to symmetry breaking and additional disturbances on the bond lengths (Ti-O) and slight distortions on the makers species (clusters) which are related to oxygen vacancies ($\text{V}_\text{O}^{\cdot\cdot}, \text{V}_\text{O}^\cdot$ and $\text{V}_\text{O}^{\cdot}$). The structural disorder at long and medium-range occurred, due to symmetry breaking by richbrookite on the TiO_2 NPs lattice and from slight distortions in the dihedral angles are presents on the clusters makers, respectively. Other hand, at short-range the TiO_2 NPs structure is more ordered due to presence of only vibrational actives-modes Raman assigned to anatase.

In fact, the oxygen vacancies might be understood as disturbances of the bond lengths (Ti-O) and distortions on the $[\text{TiO}_6]$ octahedral ascribed to the displacement of the oxygen atom position. Thus, as soon as the bulk becomes most disordered, by increases in the shift of the oxygen atom position, the oxygen vacancy changes from a neutral state ($\text{V}_\text{O}^{\cdot\cdot}$) to a slightly polarized state (V_O^\cdot and $\text{V}_\text{O}^{\cdot}$), transforming the highly ordered and neutral $[\text{TiO}_6]^\cdot$ - $[\text{TiO}_6]^\cdot$ clusters to slightly polarized and disordered $[\text{TiO}_6]^\cdot$ - $[\text{TiO}_5]$ clusters.

The distortions and deviations of both bond lengths and bond angles, between oxygen and titanium atoms on the cluster makers, increases the structural disorder which is associated with a specific type of oxygen vacancy. Each oxygen vacancy changes the concentration of the distorted and complex clusters $[\text{TiO}_6]^\cdot$, $[\text{TiO}_5, \text{V}_\text{O}^{\cdot\cdot}]$, $[\text{TiO}_5, \text{V}_\text{O}^\cdot]$ and $[\text{TiO}_5, \text{V}_\text{O}^{\cdot\cdot}]$ on the TiO_2 NPs lattice. So, this degree of structural order-disorder give rise to intermediary energy levels (shallow and deep levels) within the band gap, which the transitions between these intermediary energy levels explain the origin of the PL emissions for this system. The wide band model proposed for PL behavior at room temperature is composed by three PL sub-bands (blue, green and orange), once the green and orange components, assigned to $[\text{TiO}_5, \text{V}_\text{O}^\cdot]$ and $[\text{TiO}_5, \text{V}_\text{O}^{\cdot\cdot}]$ complex clusters, are dominant in the PL behavior. Therefore, the TiO_2 NPs

lattice contains a concentration of the clusters makers, $[\text{TiO}_5\text{V}_0^{\cdot}]$ and $[\text{TiO}_5\text{V}_0^{\cdot\cdot}]$, larger than $[\text{TiO}_6]$ and $[\text{TiO}_5\text{V}_0^x]$ species.

We believe these results will be of importance in understanding and controlling properties of the TiO_2 nanoparticles and that the reported experimental approach may be used as sources of light to understanding about the complexity of the structural defects in nanostructure system and can be relevant in addressing the open question of the degree of electron redistribution in undoped semiconducting oxides.

Acknowledgments

The authors are grateful to FAPESP 2013/07296-2, CAPES, CNPq INCTMN 573636/2008-7, Prometeo/2009/053 (Generalitat Valenciana), Ministerio de Economía y Competitividad (Spain), CTQ2012-36253-C03-02, and the Spanish Brazilian program (PHB2009-0065-PC) for financially supporting this research and for a scholarship CAPES for the scholarship (to E.S.J. and F.A.L.) and CAPES process A104/2013 to J.A.. Special thanks are given to Dr. P. Hammer (LEFE-IQ/UNESP) for help with the XPS analysis and to Dr. D. Keyson and Dr. D.P. Volanti by the development of the microwave-hydrothermal system.

References

1. A. Fujishima, K. Honda, *Nature*, 1972, **238**, 37-38.
2. D. A. Tryk, A. Fujishima, K. Honda, *Electrochim. Acta*, 2000, **45**, 2363-2376.
3. T. A. Arun, A. A. Madhavan, D. K. Chacko, G. S. Anjusree, T. G. Deepak, S. Thomas, S. V. Nair, A. S. Nair, *Dalt. Trans.*, 2014, **43**, 4830-4837.
4. K. Bourikas, C. Kordulis, A. Lycourghiotis, *Chem. Rev.*, 2014, **114**, 9754-9823.
5. J. M. Pettibone, D. M. Cwiertny, M. Scherer, V. H. Grassian, *Langmuir*, 2008, **24**, 6659-6667.
6. T. C. Jagadale, S. P. Takale, R. S. Sonawane, H. M. Joshi, S. I. Patil, B. B. Kale, S. B. Ogale, *J. Phys. Chem. C*, 2008, **112**, 14595-14602.
7. G. Li, L. Li, J. Boerio-Goates, B. F. Woodfield, *J. Am. Chem. Soc.*, 2005, **127**, 8659-8666.
8. Q. Li, B. Cheng, X. Yang, R. Liu, B. Liu, J. Liu, Z. Chen, B. Zou, T. Cui, B. Liu, *J. Phys. Chem. C*, 2013, **117**, 8516-8521.
9. H. Z. Zhang, J. F. Banfield, *J. Phys. Chem. B*, 2000, **104**, 3481-3487.
10. (a) M. Lazzeri, A. Vittadini, A. Selloni, *Phys. Rev. B*, 2001, **63**, 155409-155418; (b) A. Barnard, L. A. Curtiss, *Nano Lett.* 2005, **5**, 1291-1266. (c) A. S. Barnard, P. Zapol, L. A. Curtiss, *J. Chem. Theory Comput.* 2005, **1**, 107-116. (d) F. De Angelis, C. Di Valentin, S. Fantacci, A. Vittadini, A. Selloni, *Chem. Rev.* 2014, **114** (19), 9708-9753.
11. C. J. Howard, T. M. Sabine, F. Dickson, *Acta Crystallogr. Sec. B*, 1991, **47**, 462-468.
12. X. Chen, S. S. Mao, *Chem. Rev.*, 2007, **107**, 2891-2959.
13. J. F. Banfield, D. R. Veblen, *Am. Mineral.* 1992, **77**, 545-557.
14. M. Mattesini, J. S. de Almeida, L. Dubrovinsky, N. Dubrovinskaia, B. Johansson, R. Ahuja, *Phys. Rev. B*, 2004, **70**, 212101-212105.
15. V. Petkov, G. Holzhtüter, U. Tröge, T. Gerber, B. Himmel, *J. Non-Crystal. Sol.*, 1998, **231**, 17-30.
16. D. Reyes-Coronado, G. Rodríguez-Gattorno, M.E. Espinosa-Pesqueira, C. Cab, R. de Coss, G. Oskam, *Nanotechnology*, 2008, **19**, 145605-145615.
17. M. Galynska, P. Persson, *Inter. J. Quant. Chem.*, 2013, **113**, 2611-2620.
18. M. Landmann, T. Köhler, S. Köppen, E. Rauls, T. Frauenheim, W.G. Schmidt, *Phys. Rev. B*, 2012, **86**, 064201-0642021.
19. D. P. Macwan, N. Pragnesh Dave, S. Chaturvedi, *J. Matter. Sci.*, 2011, **46**, 3669-3686.
20. F. Peng, L. Cai, L. Huang, H. Yu, H. Wang, *J. Phys. Chem. Sol.*, 2008, **69**, 1657-1664.
21. J. Livage, C. Sanchez, *J. Non-Cryst. Sol.*, 1992, **145**, 11-19.
22. (a) T. N. Glasnov, C. O. Kappe, *Chem. Eur. J.*, 2011, **17**, 11956-11968; (b) K. Zhang, J. Dai, Y.-H. Wang, M.-H. Zeng, M. Kurmoo, *Dalt. Trans.*, 2013, **42**, 5439-5446.
23. I. Bilecka, P. Elser, M. Niederberger, *Acs Nano*, 2009, **3**, 467-477.
24. H. J. Kitchen, S. R. Vallance, J. L. Kennedy, N. Tapia-Ruiz, L. Carassiti, A. Harrison, A. G. Whittaker, T. D. Drysdale, S.W. Kingman, D. H. Gregory, *Chem. Rev.*, 2014, **114**, 1170-1206.
25. D. M. P. Mingos, D. R. Baghurst, *Chem. Soc. Rev.*, 1991, **20**, 1-47.
26. T. M. Atkins, A. Thibert, D. S. Larsen, S. Dey, N. D. Browning, S. M. Kauzlarich, *J. Am. Chem. Soc.*, 2011, **133**, 20664-20667.
27. I. Bilecka, M. Niederberger, *Nanoscale*, 2010, **2**, 1358-1374.
28. K. Manseki, Y. Kondo, T. Ban, T. Sugiura, T. Yoshida, *Dalt. Trans.*, 2013, **42**, 3295-3299.
29. L. Pan, X. Liu, Z. Sun, C.Q. Sun, *J. Mater. Chem. A*, 2013, **1**, 8299-8326.
30. M. Baghbanzadeh, L. Carbone, P. D. Cozzoli, C. O. Kappe, *Ang. Chem. Inter. Edit.*, 2011, **50**, 11312-11359.
31. D. Dallinger, C.O. Kappe, *Chem. Rev.*, 2007, **107**, 2563-2591.
32. Z. J. Luo, H. M. Li, H.M. Shu, K. Wang, J. X. Xia, Y. S. Yan, *Cryst. Growth. Des.*, 2008, **8**, 2275-2281.
33. H. M. Rietveld, *J. Appl. Crystallogr.*, 1969, **2**, 65-71.
34. A. C. Larson, R.B. Von Dreele, *Los Alamos National Laboratory Report LAUR*, 1994, 86748.
35. L.W. Finger, D.E. Cox, A.P. Jephcoat, *J. Appl. Crystal.*, 1994, **27**, 892-900.
36. F. Schossberger, *Z Kristallogr.*, 1942, **104**, 358-374.
37. R. Weyl, *Z Kristallogr.*, 1959, **111**, 401-420.
38. P. Kubelka, F. Munk-Aussig, *Zeit. Für. Tech. Phys.*, 1931, **12**, 593-601.
39. D. A. Shirley, *Phys. Rev. B* 1972, **5**, 4709-4714.
40. R. Sharma, D. P. Bisen, U. Shukla, B. G. Sharma, *Rec. Res. Sci. Tech.* 2012, **4**, 77-79
41. (a) S. R. Hall, F. H. Allen, I. D. Brown, *Acta Crystallogr., Sect. A: Found. Crystallogr.*, 1991, **47**, 655. (b) P. Thompson, D. Cox, J. Hastings, *J. Appl. Cryst.*, 1987, **20**, 79-82, 1987. (c) D. L. Bish, J. E. Post, *Am. Min.* 1993, **78**, 932-940. (d) M. Ferrari, L. Lutterotti, *J. Appl. Phys.*, 1994, **76**, 7246-7255.
42. (a) E. Jansen, W. Schafer, G. Will, *J. Appl. Cryst.*, 1994, **27**, 492-496. (b) G. Will, Powder diffraction: The Rietveld method and the two stage method to determine and refine crystal structures from powder diffraction data, Springer-Verlag Berlin Heidelberg, 2006, pp. 44-69. (c) L. Lutterotti, M. Bortolotti, G. Ischia, I. Lonardelli, H. R. Wenk, *Z. Kristallogr., Suppl.*, 2007, **26**, 125-130. (d) H. R. Wenk, L. Lutterotti, S. C. Vogel, *Powder Diffr.*, 2010, **25**, 283-296. (e) Y. Hu, H.-L. Tsai, C.-L. Huang, *J. Eur. Ceram. Soc.*, 2003, **23**, 691-696.
43. P. Tengvall, T.P. Vikingfe, I. Lundstrom, B. Liedberge, *J. Coll. Int. Sci.* 1993, **160**, 10-15.
44. S. Sahoo, A. K. Arora, V. Sridharan, *J. Phys. Chem. C*, 2009, **113**, 16927-16933.
45. Y. Lei, L. D. Zhang, J. C. Fan, *Chem. Phys. Lett.*, 2001, **338**, 231-236.
46. W. Hu, L. Li, G. Li, C. Tang, L. Sun, *Cryst. Growth. Des.*, 2009, **9**, 3676-3682.
47. A. Golubović, M. Šćepanović, A. Kremenović, S. Aškračić, V. Berec, Z. Dohčević Mitrović, Z. V. Popović, *J. Sol-Gel Sci. Technol.*, 2008, **49**, 311-319.
48. M. Šćepanović, M. Grujić-Brojčin, K. Vojisavljević, S. Bernik, T. Srećković, *J. Raman Spectrosc.*, 2012, **41**, 914-921.
49. V. Swamy, A. Kuznetsov, L. S. Dubrovinsky, R. A. Caruso, D. G. Shchukin, B. C. Muddle, *Phys. Rev. B*, 2005, **71**, 184302-184312.
50. H. Zhang, J. F. Banfield, *J. Mater. Chem.*, 1998, **8**, 2073-2076.
51. J. Muscat, V. Swamy, N. Harrison, *Phys. Rev. B*, 2002, **65**, 224112-224127.

52. C. Han, R. Luque, D. D. Dionysiou, *Chem. Commun.*, 2012, **48**, 1860-1862.
53. Y. Xie, S. H. Heo, Y. N. Kim, S. H. Yoo, S. O. Cho, *Nanotechnology*, 2010, **21**, 015303 (1-7).
54. J. I. Goldstein, D. E. Newbury, P. Echlin, D. C. Joy, A. C. Romig, C. E. Lyman, C. Fiori, E. Lifshin, Scanning Electron Microscopy and X-Ray Microanalysis, Plenum Press, New York, 1992.
55. T. Bark, J. M. K; Nowotny, *J. Chem. Phys. B*, 2006, **110**, 21560-21567
56. (a) M. K. Nowotny, T. Bark, J. Nowotny, *J. Chem. Phys. B*, 2006, **110**, 16302-16308. (b) J. Nowotny, Oxide semiconductors for solar energy conversion: titanium dioxide, Taylor & Francis Group Boca Raton, 2012, pp. 145-147. (c) J. B. Moser, R. N. Blumenthal, D. H. Whitmore, *J. Am. Ceram. Soc.* 1965, **48**, p384. (d) D-K. Lee, L-L, Jeon, M-H, Kim, W. Choi, H-I, Yoo, *Proc. Brit. Cer. Soc.* 1967, **8**, 231-245.
57. D. L. Golic, Z. Brankovic, N. Daneu, S. Bernik, G. Brankovic, *J. Sol-Gel Sci. Technol.*, 2012, **63**, 116125.
58. R.-Q. Song, H. Cölfen, *Adv. Mater.*, 2010, **22**, 1301-1330.
59. L. Zhou, P. O'Brien, *J. Phys. Chem. Lett.*, 2012, **3**, 620-628.
60. A. Pottier, C. Chanéac, E. Tronc, L. Mazerolles, J.-P. Jolivet, *J. Mater. Chem.*, 2001, **11**, 1116-1121
61. M. H. Yang, P. C. Chen, C. Tsai Mi, T. Ting Chen, I. C. Chang, H. T. Chiu, C. Y. Lee, *Cryst. Eng. Comm.*, 2014, **16**, 441-447.
62. M. R. Ranade, A. Navrotsky, H. Z. Zhang, J. F. Banfield, S. H. Elder, A. Zaban, P. H. Borse, S. K. Kulkarni, G. S. Doran, H. J. Whitfield, *Proc. Natl. Acad. Sci. USA*, 2002, **99**, 6476-6481.
63. S. Kalathil, M. M. Khan, S. A. Ansari, J. Lee, M. H. Cho, *Nanoscale*, 2013, **5**, 6323-6326.
64. K. F. Moura, J. Maul, A. R. Albuquerque, G. P. Casali, E. Longo, D. Keyson, A. G. Souza, J. R. Sambrano, I. M. G. Santos, *J. Sol Stat. Chem.*, 2014, **210**, 171-177.
65. (a) A. T. Paxton, L. Thiên-Nga, *Phys. Rev. B*, 1998, **57**, 13233-13241. (b) W. Wunderlich, L. Miao, M. Tanemura, S. Tanemura, P. Jin, K. Kaneko, A. Terai, N. Nabatova-Gabin, R. Belkada, *Inter. J. Nano.*, 2004, **3**, 439-445.
66. E. Longo, E. Orhan, F. M. Pontes, C. D. Pinheiro, E. R. Leite, J. A. Varela, P. S. Pizani, T. M. Boschi, J. F. Lanciotti, A. Beltrán, J. Andrés, *Phys. Rev. B*, 2004, **69**, 125115 (1-7).
67. L. Brus, *J. Phys. Chem.*, 1986, **90**, 2555-2560.
68. S. Feng, R. Xu, *Acc. Chem. Res.*, 2001, **34**, 239-247.
69. C. Bae, H. Yoo, M. Kim, S. Lee, H. Kim, T. K. Ahn, H. Shin, *J. Phys. Chem. C*, 2014, **118**, 9726-9732,
70. (a) G. Pirug, C. Ritke, H. P. Bonzel, *Surf. Sci.*, 1991, **241**, 289-301. (b) B. Erdem, R. A. Hunsicker, G. W. Simmons, E. D. Sudol, V. L. Dimonie, M. S. El-Aasser, *Langmuir*, 2001, **17**, 2664-2669.
71. (a) M. Murata, H. Wakino, S. Ikeda, *J. Electron. Spectros. Relat Phenon.*, 1975, **6**, 459-464. (b) C. Gao, H. Song, L. Hu, G. Pan, R. Qin, F. Wang, Q. Dai, L. Fan, L. Liu, H. Liu, *J. Lumin.*, 2008, **128**, 559-564. (c) C. D. Wagner, W. M. Riggs, L. E. Davis, J. F. Moulder, G. E. Muilenberg, Handbook of X-ray photoelectron spectroscopy: a reference book of standard data for use in x-ray photoelectron spectroscopy, Perkin-Elmer MN, Eden-Prairie, 1979. (d) Q. Xiao, L. Ouyang, L. Gao, W. Jiang, *Mater. Chem. Phys.*, 2010, **124**, 1210-1215.
72. L.-B. Xiong, J.-L. Li, B. Yang, Y. Yu, *J. Nanomat*, 2012, 831524
73. (a) P. Villards, C. D. Calvert, Pearson's Handbook of Crystallographic Data for Intermetallic Phases. American Society of Metals: Metals Park, OH, 1985. (b) A. F. Carley, P. R. Chalker, J. C. Rivieret, M. W. Roberts, *J. Chem. Soc. Farad. Trans. 1*, 1987, **83**, 351-370. (c) W. Zhang, Y. Li, S. Zhu, F. Wang, *Chem. Phys. Lett.*, 2003, **373**, 333-337. (d) S. Hashimoto, A. Tanaka, *Surf. Inter. Anal.*, 2002, **34**, 262-265.
74. D. Regonini, A. Jaroenworarluck, R. Stevens, C. R. Bowena, *Surf. Inter. Anal.*, 2010, **42**, 139-144.
75. J. F. Moulder, W. F. Stickle, P. E. Sobol, K. D. Bomben, Handbook of X-Ray Photoelectron Spectroscopy, Perkin-Elmer Corp., Eden Prairie, Minnesota, 1992.
76. A. Iwabuchi, C. Choo, K. Tanaka, *J. Phys. Chem. B*, 2004, **108**, 10863-10871.
77. R. Wang, N. Sakai, A. Fujishima, T. Watanabe, K. Hashimoto, *J. Phys. Chem. B*, 1999, **103**, 2188-2194.
78. J. P. Knauth, H. L. Tuller, *J. Appl. Phys.* 1999, **85**, 897-902.
79. (a) G. Redmond, D. Fitzmaurice, M. Graetzel, *J. Phys. Chem.*, 1993, **97**, 6951-6954. (b) G. Lu, A. Linsebigler, J. T. Yates, *J. Phys. Chem.*, 1994, **98**, 11733-11738.
80. Y. Cao, Z. Zhao, J. Yi, C. Ma, D. Zhou, R. Wang, C. Li, J. Qiu, *J. Alloy. Comp.*, 2013, **554**, 12-20.
81. (a) A. R. Albuquerque, A. Bruix, I. M. G. dos Santos, J. R. Sambrano, F. Illas, *J. Phys. Chem. C*, 2014, **118** (18), 9677-9689. (b) A. R. Albuquerque, J. Maul, E. Longo, I. M. G. dos Santos, J. R. Sambrano, *J. Phys. Chem. C*, 2013, **117** (14), 7050-7061. (c) C. Di Valentin, A. Selloni, *J. Phys. Chem. Lett.*, 2011, **2** (17), 2223-2228.
82. (a) E. Longo, E. Orhan, F. M. Pontes, C. D. Pinheiro, E. R. Leite, J. A. Varela, P. S. Pizani, T. M. Boschi, F. Lanciotti, Jr. A. Beltrán, J. Andrés, *Phys. Rev. B*, 2004, **69**, 125115 (1-7). (b) J. C. Sczancoski, L. S. Cavalcante, M. R. Joya, J. W. M. Espinosa, P. S. Pizani, J. A. Varela, E. Longo, *J. Colloid Interface Sci.*, 2009, **330**, 227-236. (c) V. M. Longo, L. S. Cavalcante, E. C. Paris, J. C. Sczancoski, P. S. Pizani, M. S. Li, J. Andrés, E. Longo, J. A. Varela, *J. Phys. Chem. C*, 2011, **115**, 5207-5219.
83. J. Marzin, J. Gérard, A. Izraël, D. Barrier, G. Bastard, *Phys. Rev. Lett.*, 1994, **73**, 716-719.
84. N. Greenham, X. Peng, A. Alivisatos, *Phys. Rev. B* 1996, **54**, 17628-17637.
85. S. J. L. Billinge, I. Levin, *Science*, 2007, **316**, 561-565.
86. (a) Y. Lei, L. D. Zhang, G. W. Meng, G. H. Li, X. Y. Zhang, C. H. Liang, W. Chen, S. X. Wang, *Appl. Phys. Lett.*, 2001, **78**, 1125-1127. (b) J. C. Yu, J. Yu, W. Ho, Z. Jiang, L. Zhang, *Chem. Mater.* 2002, **14**, 3808-3816. (c) N. Wang, H. Lin, X. Yang, L. Zhang, *J. Lumin.*, 2007, **122**, 889-891. (d) N. Serpone, D. Lawless, R. Khairutdinov, *J. Phys. Chem.*, 1995, **99**, 16646-16654.
87. <http://www.systat.com/products/PeakFit/>.
88. L. V. Saraf, S. I. Patil, S. B. Ogale, S. R. Sainkar, S. T. Kshirsager, *Int. J. Mod. Phys. B*, 1998; **12**, 2635-2647.
89. L. Forss, M. Schubnell, *Appl. Phys. B*, 1993, **56**, 363-366.
90. V. M. Longo, A. T. de Figueiredo, A. B. Campos, J. W. M. Espinosa, A. C. Hernandez, C. A. Taft, J. R. Sambrano, J. A. Varela, E. Longo, *J. Phys. Chem. A*, 2008, **112**, 8920.
91. L.S. Cavalcante, E.A.V. Ferri, J.C. Sczancoski, E.C. Paris, J.W.M. Espinosa, A.T. de Figueiredo, P.S. Pizani, V.R. Mastelaro, J.A. Varela, E. Longo, *Mat. Chem. Phys.*, 2009, **117**, 192-198
92. K. Momma, F. Izumi, *J. Appl. Cryst.*, 2011, **44**, 1272-1276.
93. L.S. Cavalcante, A.Z. Simões, J.W.M. Espinosa, L.P.S. Santos, E. Longo, J.A. Varela, P.S. Pizani, *J. Alloys Compd.*, 2008, **464**, 340-346.
94. Toyozawa, Y. Elementary Processes in Luminescence. *J. Lumin.* 1976, 12-13.
95. W. A. Weyl, T. Forland, *Ind. Eng. Chem.*, 1950, **42**, 257-263.
96. L. F. da Silva, W. Jr. Avansi, J. Andrés, C. Ribeiro, M. L. Moreira, E. Longo, V. R. Mastelaro, *Phys. Chem. Chem. Phys.*, 2013, **15**, 12386-12393
97. V. Kumar, V. Kumar, S. Som, J. H. Neethling, M. Lee, O. Ntwaeaborwa, H. C. Swart, *Nanotechnology*, 2014, **25**, 135701 (1-9).